Solution Structure of the Aminofluorene [AF]-Intercalated Conformer of the *syn*-[AF]-C^8-dG Adduct Opposite dC in a DNA Duplex†

Bing Mao,‡ Brian E. Hingerty,§ Suse Broyde,|| and Dinshaw J. Patel*,‡

Cellular Biochemistry and Biophysics Program, Memorial Sloan Kettering Cancer Center, New York, New York 10021, Health Sciences Research Division, Oak Ridge National Laboratory, Oak Ridge, Tennessee 37831, and Biology Department, New York University, New York, New York 10003

Received September 10, 1997; Revised Manuscript Received October 27, 1997⊗

ABSTRACT: We report below on a conformational equilibrium between AF-intercalated and AF-external states in slow exchange for the [AF]dG lesion positioned opposite dC in the d(C-[AF]G-C)·d(G-C-G) sequence context. The slow exchange between states is attributed to interconversion between *syn* glycosidic torsion angle in the AF-intercalated and *anti* torsion angle in AF-external conformers of the [AF]dG opposite dC containing duplex. The present paper describes an NMR-molecular mechanics study that defines the solution structure of the AF-intercalated conformer for the case of [AF]dG adduct positioned opposite dC in the d(C-[AF]G-C)·d(G-C-G) sequence context. The structure is of the base displacement-intercalation type where the aminofluorene ring is intercalated into the helix between intact Watson−Crick dG·dC base pairs, which results in a displacement of the modified guanine ring into the major groove where it stacks with the major groove edge of its 5′-flanking cytosine in the adduct duplex. The conformational equilibrium between AF-intercalated conformer (∼70%) with a *syn* alignment and AF-external conformer (∼30%) with an *anti* alignment for the [AF]dG adduct positioned opposite dC in the d(C-[AF]G-C)·d(G-C-G) sequence context can be contrasted with our earlier demonstration that the population is 100% for the AP-intercalated conformer with a *syn* alignment at the *N*-(deoxyguanosin-8-yl)-2-aminopyrene ([AP]dG) adduct site positioned opposite dC in the same sequence context [Mao, B., Vyas, R. R., Hingerty, B. E., Broyde, S., Basu, A. K., and Patel, D. J. (1996) *Biochemistry, 35*, 12659−12670]. This shift in population may reflect the much larger size of the pyrenyl ring of the [AP]dG adduct compared to the fluorenyl ring of the [AF]dG adduct which in turn might provide for a greater overlap of the aromatic amine with the flanking base pairs in the intercalated conformer of the former adduct in DNA.

The model aromatic amine carcinogens 2-aminofluorene (AF, which contains a hydrogen at the N^2-fluorenyl position) and 2-acetylaminofluorene (AAF, which contains a bulky acetyl group at the N^2-fluorenyl position) form covalent adducts at the C^8 position of guanines in DNA. The differences in the types of mutations induced by the chemically related [AF]dG and [AAF]dG carcinogens and the phenomenon of mutational hotspot base sequences are two of the most fascinating observations to emerge from structure-function studies that have addressed underlying issues in our current understanding of mutagenesis (reviewed in ref 1). The need for a molecular understanding of these observations have spurred efforts to obtain high-resolution structures of these aromatic amine carcinogen-DNA adducts in a variety of sequence contexts.

AF, which has been chemically or metabolically activated, reacts with DNA both *in vitro* and *in vivo* through covalent adduct formation with the C^8 position of guanine to generate the [AF]dG adduct **1** (Figure 1A). The bulk of the mutagenesis data indicates formation of AF-induced point mutations, especially dG to dT transversions, but other mismatches and −1 and −2 deletions are also observed in certain sequence contexts (*2*−*8*). The extensive literature on AF mutagenesis has been comprehensively reviewed (*1*, *9*). The focus of the present contributions are on the structural characterization of the [AF]dG adduct positioned opposite dC in defined sequence contexts, including the *Nar*I mutation hot spot site, in DNA.

Distinct families of structures have been elucidated by NMR studies of [AF]dG adducts as a function of sequence context and the base or lack of it positioned opposite the lesion site. The earlier studies focused on the [AF]dG adduct positioned opposite dA (*10*) and dG (*11*) in the d(C-[AF]G-C)·d(G-A/G-G) sequence context. The modified guanine with a *syn*-glycosidic torsion angle and its partner purine base were stacked within the helix while the AF ring spanned the minor groove and was directed toward the partner strand in these structures of [AF]dG·dA and [AF]dG·dG mismatch sites. Subsequent structural studies on the [AF]dG adduct positioned opposite a −1 deletion site in the d(C-[AF]G-

† This research is supported by NIH Grant CA-49982 to D.J.P., by NIH Grants CA-28038, CA-75449, and RR-06458 and DOE Grant DE-FG02-90ER60931 to S.B., and by DOE Contract DE-AC05-960R22464 with Lockheed Martin Energy Research and DOE OHER Field Work Proposal ERKP931 to B.E.H.

* Author to whom correspondence should be addressed.
‡ Memorial Sloan Kettering Cancer Center.
§ Oak Ridge National Laboratory.
|| New York University.

⊗ Abstract published in *Advance ACS Abstracts,* December 15, 1997.

S0006-2960(97)02257-5 CCC: $15.00
Published on Web 01/06/1998

A

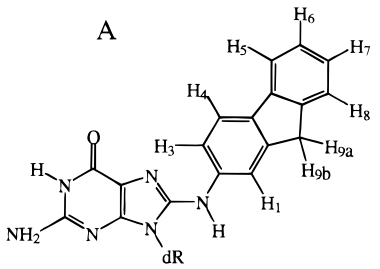

1

B

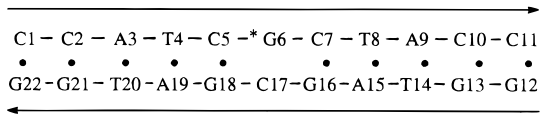

2

FIGURE 1: (A) Schematic of [AF]dG adduct **1**. (B) Schematic of the [AF]dG·dC 11-mer duplex **2**.

C)·d(G-G) sequence context (*12*) and positioned opposite a −2 deletion site in the d(C-[AF]G-A-C)·d(G-G) sequence context (*13*) established intercalation of the AF ring into the helix through base displacement of the modified *syn*-guanine into the major groove.

An important recent development was the demonstration by NMR that [AF]dG positioned opposite dC in the d(A-[AF]G-G)·d(C-C-T) sequence context adopted two conformations in slow exchange on the NMR time scale (*14*, *15*). The AF ring was positioned in the DNA major groove with all base pairs intact and the modified guanine in the *anti* conformation in one of the conformers (designated AF-external conformer). By contrast, the AF ring was intercalated into the helix accompanied by displacement of the modified guanine into the helical groove in the other conformer (designated AF-intercalated conformer). Eckel and Krugh (*15*) considered both *anti* and *syn* conformations at the [AF]dG adduct site in the AF-intercalated conformer and concluded that the *anti* conformation with displacement of the modified guanine into the minor groove best fits their data. A key conclusion of this study was that the glycosidic torsion angles were *anti* for both the AF-external and AF-intercalated conformers that were in slow exchange for [AF]-dG positioned opposite dC at the DNA oligomer duplex level (*14*, *15*).

An NMR study has also been reported for [AF]dG positioned opposite dC in the d(T-[AF]G-A)·d(T-C-A) sequence context, albeit without computational analysis of the NMR data (*16*). The authors independently observed conformational heterogenity between two AF orientations and were able to deduce structural insights into the major conformer, which contained intact base pairs and displacement of the aminoflourenyl ring in an *anti* alignment into the major groove. These conclusions have been expanded recently using ^{19}F NMR labels within the same system to establish slow exchange between a relatively undistorted B-form conformer and a highly perturbed stacked conformer separated by a 14 kcal/mol energy barrier (*17*).

Our NMR structural characterization of the [AF]dG adduct positioned opposite dC in the d(C-[AF]G-C)·d(G-C-G) sequence context has allowed us to define the structure of the AF-intercalated conformer (present paper) and at each of the three guanines in the *Nar*I mutation hot spot sequence, one of which has helped us to define the structure of the AF-external conformer (see ref *18*, the following paper in this issue). Specifically, our studies will demonstrate that the guanine is *syn* in the AF-intercalated conformer while it is *anti* in the AF-external conformer and that the slow exchange between conformers likely reflects the barrier associated with the *syn-anti* interconversion.

This paper reports on an NMR-molecular mechanics structural characterization of the [AF]dG adduct positioned opposite dC in the d(C-[AF]G-C)·d(G-C-G) sequence context in the [AF]dG·dC 11-mer duplex **2** (Figure 1B).

MATERIALS AND METHODS

Materials. *N*-Acetoxy-2-acetylaminofluorene (AAAF) was purchased from the Chemsyn Science Laboratories. The deoxyoligonucleotide d(C-C-A-T-C-G-C-T-A-C-C) and its complementary partner d(G-G-T-A-G-C-G-A-T-G-G) were synthesized on an Applied Biosystems Model 392 DNA synthesizer and purified by reverse-phase HPLC.

Preparation of Adduct. The d(C-C-A-T-C-G-C-T-A-C-C) sequence was converted into the d(C-C-A-T-C-[AF]G-C-T-A-C-C) adduct sequence as described previously (*10*). The modified d(C-C-A-T-C-[AF]G-C-T-A-C-C) 11-mer strand was annealed with the complementary unmodified d(G-G-T-A-G-C-G-A-T-G-G) 11-mer strand at 70 °C, and the stoichiometry was followed by monitoring single proton resonances in both strands.

NMR Experiments. A combination of through-space nuclear Overhauser effect (NOESY) and through-bond correlated (COSY and TOCSY) two-dimensional spectra were recorded on approximately 4 mg of the [AF]dG·dC 11-mer duplex in 0.6 mL of 0.1 M NaCl and 10 mM phosphate, pH 7.0, aqueous solution buffer and analyzed in order to assign the AF and nucleic acid protons. All experiments were carried out on Varian Unity Plus 500 or 600 MHz NMR instruments in the States-TPPI mode (*19*) with a 2.0 s relaxation delay between scans. The temperature of the sample was calibrated with an external methanol sample. The NOESY spectrum (150 ms mixing time) for exchangeable proton assignments was collected on the adduct duplex in H_2O buffer at 1 °C using a jump-return pulse for solvent suppression. The NOESY spectrum (300 ms mixing time) for nonexchangeable proton assignments was collected on the adduct duplex in D_2O buffer at 25 °C. The through-bond TOCSY data sets on the adduct duplex in D_2O buffer were recorded at spin lock times of 40 and 80 ms at 25 °C.

Several factors went into the conversion of the NOE intensities into the distance bounds used for the structure determination of the adduct duplex. Distance restraints involving nonexchangeable protons were estimated from NOE build-up curves of NOESY spectra recorded at 50, 100, 150, and 200 ms on the adduct duplex in D_2O at 25 °C. The interproton distance calculations were based on the isolated two-spin approximation using the dT(NH3)-dA(H2) fixed distance of 2.92 Å for the NOESY spectrum (single mixing time) in H_2O and the dC(H6)-dC(H5) fixed distance of 2.45 Å for the NOESY data sets (four mixing times) in D_2O solution. A quadratic polynomial was fitted to the data points, and the initial slope was calculated from the linear

fit of the quadratic curves to the first non-zero mixing time. The upper and lower bound ranges on the estimated interproton distances for nonexchangeable protons were determined based on the resolution of the cross-peaks in the two-dimensional contour plots and the quality of the NOE build-up plots. The base proton to sugar H1′ NOE cross-peaks in the shortest mixing time NOESY data set in D_2O were evaluated to qualitatively differentiate between *syn* (strong NOE)- and *anti* (weak NOE)-glycosidic torsion angles (*20*).

The proton−proton vicinal coupling constants among sugar protons were analyzed from phase-sensitive COSY spectra to qualitatively distinguish between the C3′-*endo* and C2′-*endo* family of sugar puckers. The relative intensity of the NOE cross-peaks between base protons and their own and 5′-flanking sugar H2′, H2″ and H3′ protons were used to qualitatively distinguish between the A and B family of helices for the modified duplex (*21*).

Molecular Mechanics Computations. Minimized potential energy calculations were carried out with DUPLEX, a molecular mechanics program for nucleic acids that performs potential energy minimizations in the reduced variable domain of torsion angle space (*22*). DUPLEX uses a potential set similar to the one developed by Olson and co-workers for nucleic acids (*23*). Geometry and force field parameters, including partial charges, for the [AF]dG adduct were the same as those employed previously (*24*, *25*). A hydrogen-bond penalty function (*22*) was employed in all first stage minimizations to aid the minimizer in locating the Watson−Crick hydrogen-bonded structures indicated by the NMR data. To locate minimum energy conformations with interproton distances available from the experimental NMR data, pseudopotentials (permitting upper and lower bound restraints) were added to the energy, as described previously (*10*, *26*, *27*). Briefly, the following functions were used:

$$F_N = W_N \sum_1^n (d - d_N)^2 \quad (1)$$

$$F_{NN} = W_{NN} \sum_1^n (d - d_{NN})^2 \quad (2)$$

The Ws are adjustable weights (in the range 10−30 kcal/mol Å^2). d is the current value of the interproton distance, d_N is a target upper bound, and d_{NN} a target lower bound. Equation 1 is implemented when d is greater than d_N, and eq 2 is implemented when d is less than d_{NN}. The functions are summed over all n target distances. All penalty functions were released in the last minimization steps to yield unrestrained final structures that are minimum energy conformations. F_N and F_{NN} can also be employed as relative indices of goodness-of-fit to the NMR data. Here the d values are the achieved distances in a given model and the Ws are the weights employed in the search, 15 kcal mol^{-1} Å^{-2} in the present work. F_N and F_{NN} are composites, reflecting the overall fit of all the achieved distances to their targets. They both adopt values of zero when all model distances are within the upper and lower NMR distance bounds. Small deviations from the NMR targets, within the uncertainty of the data, are accepted in computed models, and these therefore have non-zero F_N and F_{NN} values.

Our search strategy employs a set of key NMR distance restraints, together with information from the NMR data on the hydrogen bonding pattern between bases for the hydrogen-bond penalty function. NMR information about the glycosidic torsion angle and the deoxyribose sugar pseudorotation parameter are also included. The resulting structures are ranked according to energy and goodness-of-fit (eqs 1 and 2). At this point, the first set of NMR assigned distance bounds are evaluated in relation to achieved distances and energies in the ensemble of 16 structures. Cross-checks involving distances not employed as restraints and satisfaction of other criteria such as chemical shifts are also made. Especially in the case of conformational heterogeneity, this affords feedback to the NMR analysis and offers the opportunity for reassessment of the distance bounds. This procedure can be carried out iteratively until structures of lowest energy and best goodness-of-fit are located.

Computations were carried out at the Department of Energy's National Energy Research Supercomputer Center and the National Science Foundation's San Diego Supercomputer Center.

RESULTS

Conformational Equilibrium. The varying intensities of imino protons in the 10.0−14.5 ppm region of the spectrum of the [AF]dG·dC 11-mer duplex in H_2O buffer at 1 °C (Figure 2A) establish the existence of more than one conformer in slow exchange at this temperature. This conclusion is supported by the observation of chemical exchange cross-peaks in NOESY spectra of the adduct duplex in H_2O and D_2O solution (see below). The imino protons of [AF]dG6 and flanking dG16 and dG18 resonate to high field (Figure 2A), as do the corresponding nonexchangeable AF protons in the major conformer of the [AF]dG·dC 11-mer duplex. This conformer is of the AF-intercalated type since these NMR markers exhibit spectral characteristics similar to what has been reported previously for the intercalated aminopyrenyl ring of the [AP]dG adduct positioned opposite dC in the same sequence context in the [AP]-dG·dC 11-mer duplex (*28*). The minor conformer in the equilibrium is of the AF-external type based on the downfield chemical shifts for the imino protons centered about the lesion site and the downfield chemical shifts of the AF protons in the adduct duplex (see below and ref 18). A measurement of the intensities of the resolved dG18 imino proton in the two conformers of the adduct duplex at 1 °C (Figure 1A) establishes a ratio of ∼70% AF-intercalated and ∼30% AF-external conformers in slow equilibrium for the [AF]dG·dC 11-mer duplex in the d(C-[AF]G-C)·d(G-C-G) sequence context.

Exchangeable Nucleic Acid Protons. The exchangeable proton NMR spectrum (10−14.5 ppm) of the [AF]dG·dC 11-mer in H_2O buffer, pH 7.0 at 1 °C, is plotted in Figure 2A. Three upfield shifted resonances at 10.90, 11.70, and 12.11 ppm are observed along with the partially resolved imino resonances between 12.7 and 13.6 ppm in the spectrum of the major conformer of the adduct duplex. These imino proton assignments were determined following an analysis of NOE connectivities with nearby protons both across the base pair and to the flanking base pairs in the adduct duplex (reviewed in refs 21 and 29).

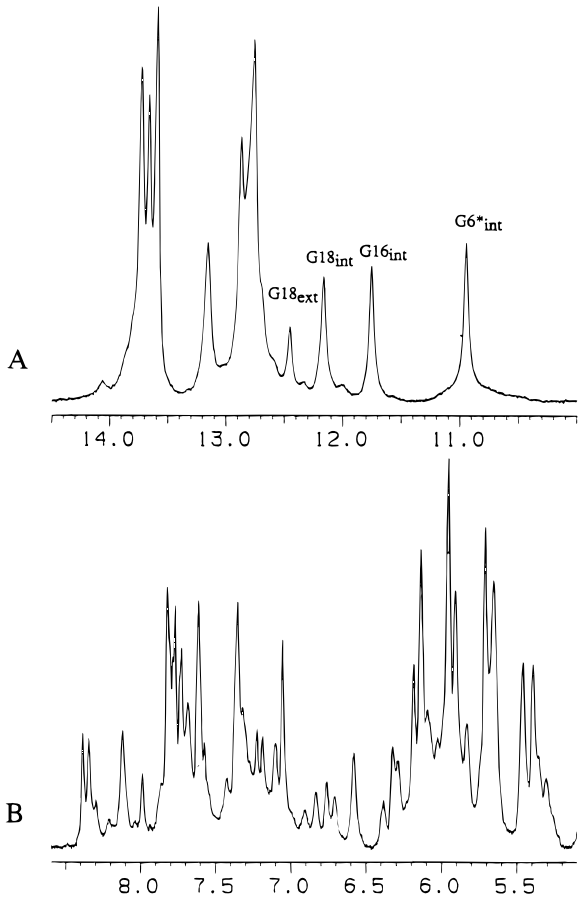

FIGURE 2: Proton NMR spectra of the [AF]dG·dC 11-mer duplex in 0.1 M NaCl, 10 mM phosphate, and 0.1 mM EDTA in aqueous solution, pH 7.0. (A) Exchangeable imino proton spectrum (10−14.5 ppm) in H_2O buffer at 1 °C. Selective imino proton assignments are listed over the spectrum. (B) The nonexchangeable proton spectrum (5.1−8.6 ppm) in D_2O buffer at 25 °C.

An expanded NOESY (150 ms mixing time) contour plot of the symmetrical 10.5−14.0 ppm imino proton region (Figure 3C) establishes connectivities between adjacent base pairs in the [AF]dG·dC 11-mer duplex from the dC2·dG21 pair located toward one end of the helix to the dC5·dG18 pair located 5′ to the [AF]dG6·dC17 modified pair and from its 3′- neighbor dC7·dG16 pair to the dC10·dG13 pair located toward the opposite end of the helix. The sequential connectivities for the terminal base pairs dC1·dG22 and dC11·dG12 are not observed presumably due to fast exchange of the imino protons of dG12 and dG22 with H_2O. The NOE connectivities between the imino protons of dG16, [AF]dG6, and dG18 are not observed, although these residues correspond to adjacent positions along the duplex sequence.

An expanded plot of the 150 ms mixing time NOESY spectrum of the [AF]dG·dC 11-mer duplex correlating NOE connectivities between the imino protons (10.5−14.0 ppm) and the base and amino protons (4.8−8.7 ppm) is plotted in Figure 3B. The observed NOE patterns establish Watson-Crick base pairing at all dA·dT pairs (thymine imino to adenine H2 protons, peaks D to G, Figure 3B) and at all dG·dC pairs (guanine imino to cytosine amino protons), as shown for the dC5·dG18 and dC7·dG16 pairs (peaks A, A′ and B, B′, respectively, Figure 3B), with the exception of the alignment of the [AF]dG6 adduct positioned opposite dC17 at the modification site (Figure 3B).

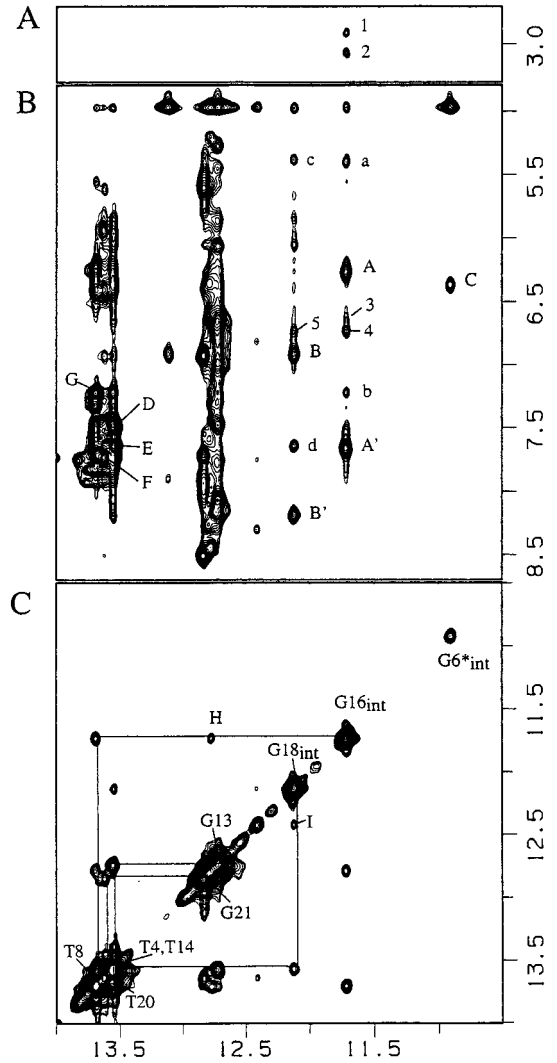

FIGURE 3: Expanded NOESY (150 ms mixing time) contour plots of the [AF]dG·dC 11-mer duplex in H_2O buffer at 1 °C. (A) NOEs between imino proton (10.5−14.0 ppm) and AF methylene protons (2.7−3.3 ppm). (B) NOE connectivities between the imino protons (10.5−14.0 ppm) and the nucleic acid base and amino protons and the aminopyrene protons (4.8−8.7 ppm). The cross-peaks A, A′ and B, B′ designate guanine imino to cytosine amino proton connectivities across Watson−Crick dG·dC pairs and are assigned as follows: A, A′, dG16(NH1)-dC7(NH_2-4e,b); B, B′, dG18(NH1)-dC5(NH_2-4e,b). The cross-peak between the [AF]dG6 imino proton and its own amino protons is designated C. The cross-peaks D−G designate thymine imino to adenine H2 protons connectivities across Watson−Crick dA·dT pairs and are assigned as follows: D, dT14-(NH3)-dA9(H2); E, dT4(NH3)-dA19(H2); F, dT20(NH3)-dA3(H2); and G, dT8(NH3)-dA15(H2). The NOE cross-peaks a−d designate additional connectivities between the imino protons of dG16 and dG18 to surrounding nucleic acid protons and are assigned as follows: a, dG16(NH1)-dC7(H5); b, dG16(NH1)-dA15(H2); c, dG18(NH1)-dC5(H5); d, dG18(NH1)-dA19(H2). The intermolecular NOE cross-peaks 1−5 between nucleic acid and AF protons are assigned as followed: 1 and 2, dG16(NH1)-AF(H9a,b); 3, dG16(NH1)-AF(H5); 4, dG16(NH1)-AF(H4); 5, dG18(NH1)-AF-(H4). (C) NOE connectivities between adjacent base pairs in the symmetrical 10.5−14.0 ppm region are traced starting at dG21 located at one end of the helix and proceeding to dG18 located 5′ to [AF]dG6 and from dG16 located 3′ to [AF]dG6 and proceeding toward dG13 located at the other end of the helix (solid lines). The diagonal cross-peaks corresponding to the imino protons of dT8, dT20, dT4, dT14, dG21, dG13, dG18, dG16, and [AF]dG6 are labeled. The cross-peak labeled H and I designate exchange cross-peaks of dG16(NH1) and dG18(NH1), respectively, between the major AF-intercalated and minor AF-external conformers.

Table 1: Proton Chemical Shifts of the Major AF-Intercalated Conformer of the d(T4-C5-[AF]G6-C7-T8)·d-(A15-G16-C17-G18-A19) Segment of the [AF]dG·dC 11-mer Duplex in Aqueous Buffer

	exchangeable proton chemical shifts (ppm) at 1 °C		
	G(NH1)/T(NH3)	G(NH_2-2)	C(NH_2-4)
dT4·dA19	13.55		
dC5·dG18	12.11		8.17,[a] 6.90[b]
[AF]dG6·dC17	10.90	6.36	
dC7·dG16	11.70		7.65,[a] 6.27[b]
dT8·dA15	13.69		

	nonexchangeable proton chemical shifts (ppm) at 25 °C					
	H8/H6	H2/H5/CH_3	H1′	H2′,H2″	H3′	H4′
dT4	7.17	1.49	5.82	2.10, 2.39	4.81	4.27
dC5	7.07	5.43	5.86	1.67, 2.47	4.69	4.13
[AF]dG6	na		5.73	3.71, 2.14	4.90	4.24
dC7	7.66	5.44	6.05	2.12, 2.49	4.83	4.30
dT8	7.36	1.57	5.62	2.12, 2.42	4.87	4.17
dA15	8.08	7.27	5.96	2.67, 2.77	5.02	4.38
dG16	7.26		5.32	2.28, 2.36	4.96	4.27
dC17	8.07	6.23	6.41	2.29, 2.70	4.97	4.27
dG18	6.99		5.30	2.36, 2.51	4.69	4.13
dA19	7.96	7.65	6.11	2.47, 2.80	4.92	4.38

[a] Hydrogen-bonded amino proton. [b] Exposed amino proton. na Not available.

The upfield shifted imino proton at 10.90 ppm is assigned to [AF]dG6 based on an NOE to its own averaged amino protons at 6.36 ppm (peak C, Figure 3B) and an exchange cross-peak with the H_2O resonance in the adduct duplex. We do not detect NOEs between the imino proton of [AF]-dG6 and other imino and nonexchangeable protons in the NOESY contour plots of the adduct duplex. Its upfield shift and rapid exchange with H_2O suggests that the guanine imino proton of [AF]dG6 is most likely looped out of the helix and not hydrogen bonded to its partner dC17 in the [AF]-dG·dC 11-mer duplex.

The imino proton at 12.45 ppm is assigned to dG18 in the minor AF-external conformer (Figure 2A) since a chemical exchange cross-peak (peak I, Figure 3C) is detected to the assigned 12.11 ppm imino proton of dG18 in the major AF-intercalated conformer in the NOESY spectrum of the adduct duplex in H_2O solution. Further, a chemical exchange cross-peak (peak H, Figure 3C) is also observed between the assigned imino proton of dG16 in the major AF-intercalated conformer and the imino proton at 12.78 ppm, which is assigned to dG16 in the minor AF-external conformer. The chemical shift difference between the AF-intercalated and AF-external conformers is more pronounced for the imino proton of dG16 (1.08 ppm) than dG18 (0.34 ppm) in the adduct duplex.

The exchangeable imino and amino proton chemical shifts are listed for the central d(T4-C5-[AF]G6-C7-T8)·d(A15-G16-C17-G18-A19) segment of the [AF]dG·dC 11-mer duplex at 1 °C in Table 1 and for the entire adduct duplex in Table S1 (Supporting Information). Relative to the control 11-mer duplex, upfield shifts are observed for the imino protons of [AF]dG6 (−1.93 ppm), dG16 (−1.04 ppm), and dG18 (−0.56 ppm), and the amino protons of dC7 (−0.51 and −0.28 ppm for the bound and exposed protons, respectively) in the major AF-intercalated conformer of the [AF]dG·dC 11-mer duplex.

Nonexchangeable Nucleic Acid Protons. The base and sugar H1′ nonexchangeable proton spectrum region (5.1−8.6 ppm) of the [AF]dG·dC 11-mer duplex in D_2O buffer, pH 7.0 at 25 °C is shown in Figure 2B. Nonexchangeable proton assignments are based on an analysis of through space NOESY data sets (50 and 300 ms mixing times) and through bond COSY and TOCSY data sets (40 and 80 ms spin lock times) at 25 °C (reviewed in refs 21 and 29).

The expanded NOESY (300 ms mixing time) contour plot establishing sequential connectivities between the base protons (6.5−8.5 ppm) and the sugar H1′ and cytosine H5 protons (4.8−6.4 ppm) of the [AF]dG·dC 11-mer duplex in D_2O buffer, pH 7.0 at 25 °C is plotted in Figure 4A. The base to sugar H1′ proton connectivities are traced from dA3 to dA9 along the modified strand (solid line, Figure 4) and from dT14 to dT20 along the complementary strand (dashed line, Figure 4) in the adduct duplex. The interruption in the tracing at the dC5-[AF]dG6 step on the modified strand is due to the absence of a purine H8 proton following AF modification at the C^8 position of dG6 in the adduct duplex. A break in connectivity is also observed at the dC17-dG18 step (see box, Figure 4A) on the unmodified complementary strand of the adduct duplex. These base and H1′ sugar assignments have been confirmed by cross-checks in other regions of the NOESY plot (Figure 5A), as well as from COSY (Figure 5B) and TOCSY plots to yield a complete set of sugar H2′, H2″, H3′, and H4′ proton assignments in the adduct duplex. The chemical shifts of the nonexchangeable nucleic acid protons are listed for the d(T4-C5-[AF]-G6-C7-T8)·d(A15-G16-C17-G18-A19) segment of the [AF]-dG·dC 11-mer duplex in Table 1 and for the entire adduct duplex in Table S2 (Supporting Information).

Numerous unusual chemical shifts are observed for the nonexchangeable nucleic acid protons in the adduct duplex, relative to the control unmodified 11-mer duplex. Upfield chemical shifts are observed for the major groove dC5(H5) (−0.33 ppm) base and dC5(H2′) (−0.33 ppm), and dC7-(H2′) (−0.30 ppm) sugar protons of the modified strand and for the dG16(H8) (−0.37 ppm) and dG18(H8) (−0.86 ppm) base and dG16(H1′) (−0.35 ppm), and dG18(H1′) (−0.31 ppm) sugar protons of the complementary strand on adduct formation. Further, downfield chemical shifts are observed at the H6 (+0.89 ppm) and H5 (+1.06 ppm) base and H1′ (+0.83 ppm), H2′ (+0.46 ppm), and H2″ (+0.42 ppm) sugar protons of the partner dC17 residue on adduct formation. The exchangeable and nonexchangeable proton chemical shift changes on proceeding from the control duplex to the adduct duplex for the central d(T4-C5-[AF]G6-C7-T8)·d-(A15-G16- C17-G18-A19) segment are summarized in Table S3 (Supporting Information).

The magnitude of the NOE between the purine H8 proton and its own sugar H1′ proton provides a direct distinction between *syn*- and *anti*-glycosidic torsion angle at purine residues with a strong NOE observed for *syn* alignments (corresponding to interproton distance of ∼2.5 Å) and a weak NOE observed for *anti* alignments (corresponding to interproton distance of ∼3.7 Å) as first pointed out for Z-DNA (*20*). Unfortunately, the H8 proton is missing in the C^8-modified [AF]dG adduct, and an alternate approach based on proton chemical shifts has been used to attempt to distinguish between *syn* and *anti* alignments at the [AF]dG residue in the AF-intercalated conformer of the [AF]dG·dC

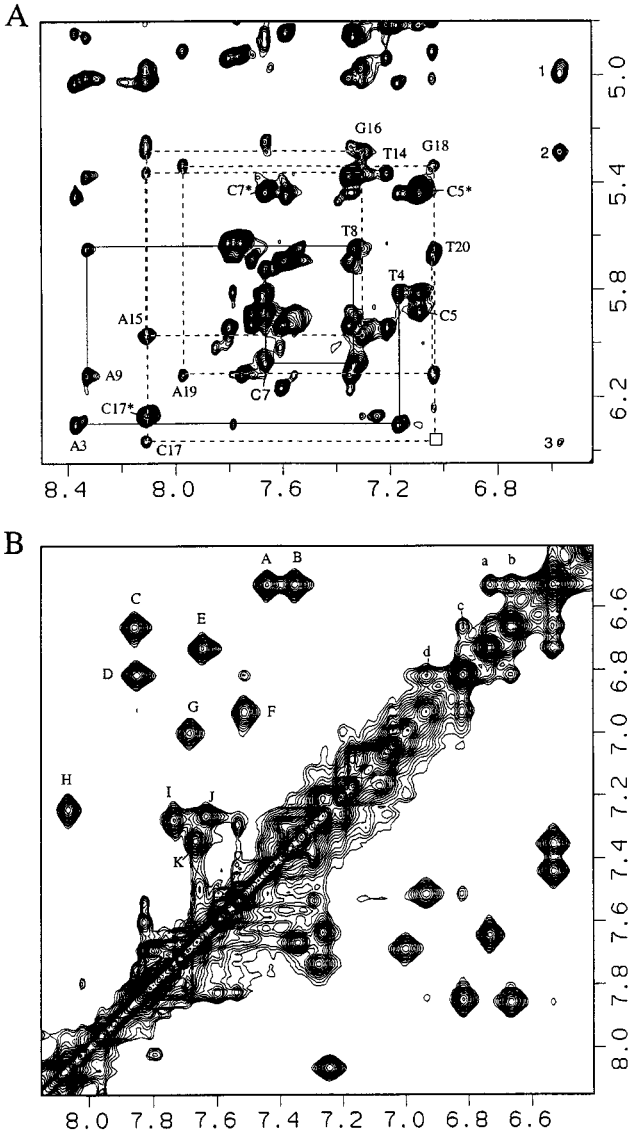

FIGURE 4: (A) Expanded NOESY (300 ms mixing time) contour plot of the [AF]dG·dC 11-mer duplex in D_2O buffer at 25 °C establishing distance connectivities between the base (purine H8 and pyrimidine H6) protons (6.45−8.5 ppm) and the sugar H1′ and cytosine H5 protons (4.8−6.45 ppm) for the d(A3-T4-C5-[AF]G6-C7-T8-A9)·d(T14-A15-G16-C17-G18-A19-T20) segment. The NOE connectivities between the base and their own and 5′-flanking sugar H1′ protons are traced from dA3 to dA9 on the modified strand (solid line), with a break in connectivity at the dC5-[AF]dG6 step due to the absence of H8 proton for [AF]dG6, and from dT14 to dT20 on the unmodified complementary strand (dashed line), with the break in connectivity at the dC17-dG18 step (boxed region). The cross-peaks between cytosine H5 and H6 protons are designated by asterisks. The cross-peaks numbered 1−3 identify intermolecular AF-DNA NOEs and are assigned as follows: 1, AF(H6,H7)-dC17-(H3′); 2, AF(H6,H7)-dG16(H1′); 3, AF(H6,H7)-dC17(H1′). (B) Expanded NOESY (100 ms mixing time) contour plot of the [AF]-dG·dC 11-mer duplex in D_2O buffer at 25 °C. Chemical exchange cross-peaks are labeled with capital letters A−K and are assigned as follows: A, AF($H6_{ext}$)-AF($H6_{int}$); B, AF($H7_{ext}$)-AF($H7_{int}$); C, AF-($H5_{ext}$)-AF($H5_{int}$); D, AF($H4_{ext}$)-AF($H4_{int}$); E, AF($H8_{ext}$)-AF($H8_{int}$); F, AF($H3_{ext}$)-AF($H3_{int}$); G, dG18($H8_{ext}$)-dG18($H8_{int}$); H, dC17-($H6_{int}$)-dC17($H6_{ext}$); I, AF($H1_{ext}$)-AF($H1_{int}$); J, dG16($H8_{ext}$)-dG16-($H8_{int}$); K, dC7($H6_{int}$)-dC7($H6_{ext}$). The cross-peaks a−d designate NOEs between AF protons and are assigned as follows: a: AF-(H8)-AF(H6,H7); b, AF(H5)-AF(H6,H7); c, AF(H4)-AF(H5); d, AF(H3)-AF(H4).

11-mer duplex. The validation of this proton chemical shift approach is based on an earlier study of the (+)-*trans-anti*-[BP]dG adduct positioned at a template-primer junction (*30*). The H8 proton is available in the N^2-[BP]dG adduct and the observed strong H8 to its own H1′ NOE established formation of a *syn* alignment at the [BP]dG adduct in this junctional sequence context. Significantly, the *syn* alignment at the [BP]dG adduct site resulted in a selective greater than 1 ppm downfield shift of its H2′ proton (resonates at 3.67 ppm), suggesting that this could prove to be a useful marker for *syn* alignments of guanines and modified guanines in DNA. Indeed, similar large downfield shifts of guanine H2′ protons have also been reported for nonterminal *syn*-guanines that participate in G-tetrad formation in G-quadruplexes (*31*, *32*).

We observe an inversion in the characteristic H2′ and H2″ sugar cross-peak patterns at the lesion site with the H2′ proton (3.71 ppm) of [AF]dG6 shifting dramatically downfield in the [AF]dG·dC 11-mer duplex (Figure 5). We interpret this large downfield shift of the H2′ proton of the AF-adducted guanine in the AF-intercalated conformer to be consistent with a *syn*-glycosidic torsion angle at the [AF]-dG6 residue in the [AF]dG·dC 11-mer duplex.

Nonexchangeable Aminofluorene Protons. The nonexchangeable aminofluorene protons in the major AF-intercalated conformer were assigned from an analysis of the through-space NOE patterns (Figure 4B) and through-bond coupling connectivities in the [AF]dG·dC 11-mer duplex. We detect exchange cross-peaks between the assigned nonexchangeable aminofluorene protons in the major AF-intercalated conformer and their counterparts in the minor AF-external conformer (peaks A−K, Figure 4B) in the expanded NOESY contour plot (100 ms mixing time) within the symmetrical 6.4−8.2 ppm region of the [AF]dG·dC 11-mer duplex in D_2O buffer at 25 °C. These nonexchangeable aminofluorene proton chemical shifts in the major AF-intercalated and minor AF-external conformers of the [AF]-dG·dC 11-mer duplex are listed in Table 2 and compared to the corresponding values in the [AF]dG·del duplex containing a −1 deletion site published previously (*12*) in Figure 6. The aromatic aminofluorene ring protons resonate between 7.5 and 8.0 ppm in the AF-external conformer (closed circles, Figure 6) and shift upfield between 6.5 and 7.0 ppm in the AF-intercalated conformer (open circles, Figure 6) of the [AF]dG·dC 11-mer duplex. A similar upfield shift is observed for the aminofluorene protons of [AF]dG positioned opposite a −1 deletion site (open squares, Figure 6) in which the aminofluorene ring intercalates between flanking dG·dC base pairs (*12*).

Intermolecular NOEs in the [AF]dG·dC 11-mer Duplex. A set of intermolecular AF-DNA NOE cross-peaks have been identified in the NOESY spectra of the [AF]dG·dC 11-mer duplex (Table 3). Some of these intermolecular AF-DNA NOE cross-peaks are labeled by numbers in the expanded NOESY plots of the exchangeable protons in H_2O solution (Figure 3) and nonexchangeable protons in D_2O solution (Figures 4 and 5), and the assignments are listed in the figure captions.

The distribution of proton distance restraints is such that they are restricted to NOEs between the protons of the AF ring and the d(C5-[AF]G6-C7)·d(G16-C17-G18) segment of the adduct duplex (Table 3). The majority of the NOE cross-peaks associated with nonexchangeable protons involve the overlapped aminofluorene H6 and H7 protons with neigh-

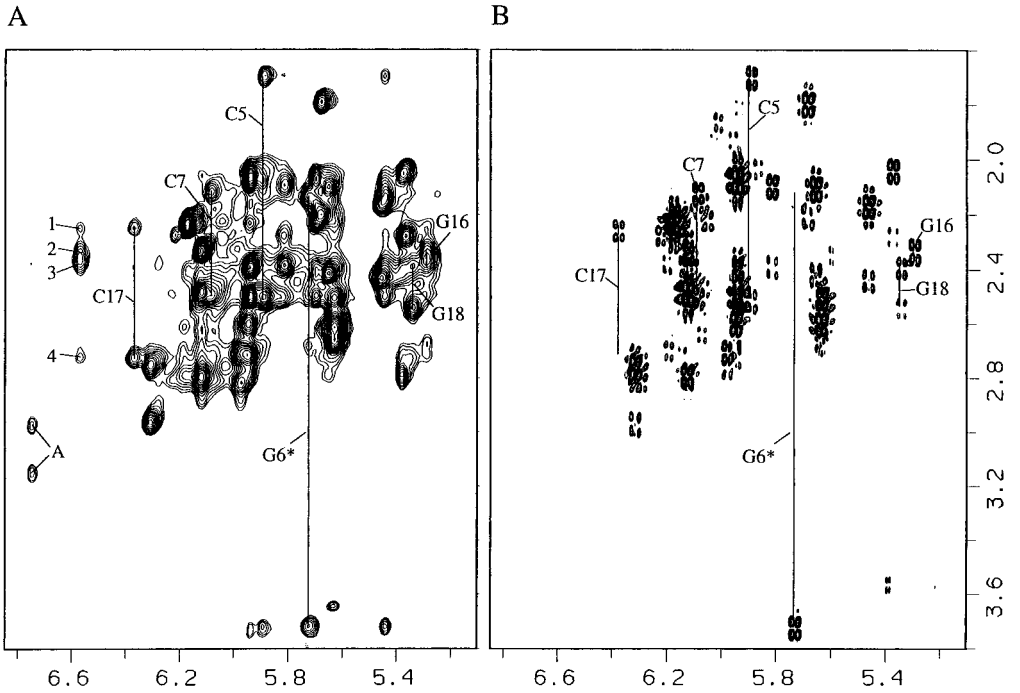

FIGURE 5: (A) An expanded NOESY (300 ms mixing time) contour plot of the [AF]dG·dC 11-mer duplex in D_2O buffer at 25 °C showing NOEs between the sugar H1′ protons (5.1−6.85 ppm) and H2′, H2″ protons (1.9−3.8 ppm). The NOE cross-peak A is assigned to AF-(H8)-AF(H9a,b). The intermolecular AF-DNA NOE cross-peaks 1−4 are assigned as follows: 1, dG17(H2′)-AF(H6,H7); 2, dG16(H2″)-AF(H6,H7); 3, dG16(H2′)-AF(H6,H7); 4, dC17(H2″)-AF(H6,H7). (B) An expanded phase sensitive COSY contour plot of the [AF]dG·dC 11-mer duplex in D_2O buffer at 25 °C establishing coupling connectivities between the H1′ protons (5.1−6.85 ppm) and H2′, H2″ protons (1.9−3.8 ppm). In both panels A and B, the H2′ and H2″ protons of dC5, [AF]dG6, dA7, dC8, dG17, and dG18 are connected by lines and labeled. The H2′ protons resonate upfield of the H2″ protons for the majority of these residues except for [AF]dG6 and dG16 where the H2″ protons resonate upfield of the H2′ proton.

Table 2: Chemical Shift Values (ppm) of the Aminofluorene Protons in the [AF]dG·dC 11-mer Duplex at 25 °C

proton	AF-external	AF-intercalated
AF(H1)	7.73	7.27
AF(H3)	7.52	6.93
AF(H4)	7.85	6.82
AF(H5)	7.86	6.66
AF(H6)	7.44	6.53
AF(H7)	7.35	6.53
AF(H8)	7.65	6.73
AF(H9a,b)	3.97, 3.97	2.98, 3.14

boring DNA protons. Separate calculations were performed to derive the upper and lower bounds of the NMR-derived intermolecular AF-DNA distance restraints involving these two superpositioned AF protons assuming the NOE intensities were contributed either by one of the two protons or by both protons; the final assigned upper and lower bounds were taken from the lower and upper limits of the separate calculations (Table 3). The NOE cross-peaks involving the broad dC17 sugar protons exhibit weak intensities, reflecting potential conformational heterogeneity associated with the alignment of dC17 positioned opposite the lesion site.

Carbon Spectra. The expanded contour plot of a natural abundance proton-carbon HMQC correlation experiment that correlates the H1′ and C1′ chemical shifts of individual residues for the [AF]dG·dC 11-mer duplex in D_2O buffer at 25 °C is plotted in Figure 7A. The carbon resonances are assigned on the basis of the known H1′ proton assignments in the adduct duplex. The C1′ chemical shift assignments for residues in the d(T4-C5-[AF]G6-C7-T8)·d(A15-G16-C17-G18-A19) segment in the adduct duplex are labeled in

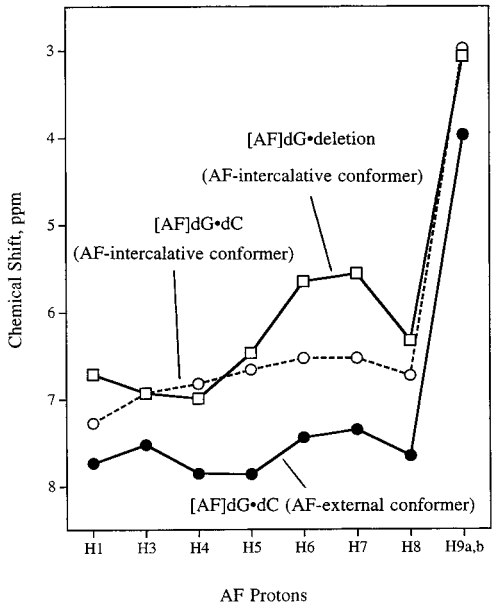

FIGURE 6: Plot comparing the aminofluorene ring proton chemical shifts for AF-intercalated conformer (open circles) and AF-external conformer (closed circles) in the [AF]dG·dC 11-mer duplex reported in this study, and the AF-intercalated conformer in the [AF]dG·1 del 11-mer duplex (open squares) reported previously (*12*).

Figure 7A except for the dC17 residue due to the broad nature of this resonance. We note that the C1′ chemical shift of [AF]dG6 (86.11 ppm) is downfield relative to other assignable dG residues in this segment of the adduct duplex (Figure 7A). It has been previously established that downfield sugar C1′ carbon chemical shifts that can range up to 5 ppm are observed for DNA residues adopting *syn* glyco-

Table 3: Comparison of Experimental Distance Restraints with Those Observed for the NMR-Molecular Mechanics Structure of the [AF]dG·dC 11-mer Duplex

	interproton distances (Å)		
	exptl bounds	observed (I)	observed (II)
Exchangeable Protons			
[AF]dG6(NH1)-dC5(H3′)	4.0−6.0	5.47	5.25
dG16(NH1)-AF(H4)	3.0−4.5	4.35	3.03
dG16(NH1)-AF(H5)	4.0−6.0	4.17	3.73
dG16(NH1)-AF(H9a,b)	4.0−6.0	3.64, 4.91	5.91, 5.03
dG18(NH1)-AF(H4)	4.0−6.0	4.73	5.78
Nonexchangeable Protons[a]			
dC17(H5)-dG16(H3′)	2.8−5.2	2.82	4.04
dG16(H1′)-AF(H6/H7)	2.6−5.4	3.86, 3.50	3.55, 5.27
dG16(H2′)-AF(H6/H7)	2.2−4.6	2.35, 3.23	2.42, 3.18
dG16(H2″)-AF(H6/H7)	2.1−4.3	2.91, 2.38	2.34, 4.11
dG16(H4′)-AF(H6/H7)	2.6−5.5	5.78, 5.51	5.64, 6.80
dG16(H8)-AF(H6/H7)	2.6−5.4	3.92, 5.49	3.68, 3.38
dG16(H8)-AF(H5)	3.4−5.5	4.97	5.33
dC17(H1′)-AF(H6/H7)	2.6−5.4	2.54, 3.69	3.65, 5.40
dC17(H2″)-AF(H6/H7)	3.0−6.0	4.78, 5.39	5.33, 6.93
dC17(H3′)-AF(H6/H7)	2.7−5.7	5.36, 4.79	5.88, 7.94
dC17(H4′)-AF(H6/H7)	2.8−5.9	3.60, 2.31	4.55, 6.88
dG18(H8)-AF(H6/H7)	2.6−5.4	5.27, 5.87	6.30, 7.65

[a] The resonances of the aminofluorene protons H6 and H7 are overlapped; therefore, wide experimental bounds were given for distances involving these protons.

sidic torsion angles, provided that they retain C2′-*endo* sugar pucker geometries (*33*, *34*). We detect a strong coupling cross-peak between the H1′ (5.73 ppm) and H2′ (3.71 ppm) protons of [AF]dG6 (Figure 5B), placing this sugar within the C2′-*endo* range. The smaller magnitude of the downfield sugar C1′ carbon chemical shift of [AF]dG6 does not permit a definitive differentiation between *syn* and *anti* glycosidic torsion angles at this modified residue in the [AF]dG·dC 11-mer duplex.

Phosphorus Spectra. The proton decoupled phosphorus spectrum of the [AF]dG·dC 11-mer duplex has been recorded in D_2O buffer at 25 °C. The phosphorus resonances are dispersed over a 1.5 ppm range with two resonances shifted to low field of the −3.5 to −4.5 ppm spectral region. The phosphorus resonances have been assigned from an analysis of the proton detected phosphorus-proton heteronuclear correlation experiment with the expanded contour plot shown in Figure 7B. Several phosphorus resonances can be correlated to the 5′-linked H3′ proton and the 3′-linked H4′ and H5′,5″ protons. The phosphorous chemical shifts for the [AF]dG6-dC7 (−2.66 ppm) and dG16-dC17 (−3.20 ppm) steps that are centered about the lesion site are shifted to low field of the −3.5 to −4.5 ppm unperturbed phosphodiester backbone chemical shift range.

Molecular Mechanics Computations. The conformational search strategy employed in the molecular mechanics program DUPLEX began with a B-DNA (*35*) central d(T4-C5-[AF]G6-C7-T8)·d(A15-G16-C17-G18-A19) 5-mer segment of the [AF]dG·dC 11-mer duplex. In these trials, the DUPLEX hydrogen-bond penalty function (*22*) for Watson−Crick base pairing was utilized at all base pairs except at the lesion site, since the NMR data indicated that the [AF]-dG6·dC17 base pair was denatured and NMR derived upper and lower bound distance restraints involving intermolecular AF-DNA interactions (Table 3) were included. The DNA starting conformation was B-form except for a *syn* ($\chi = 60°$)-

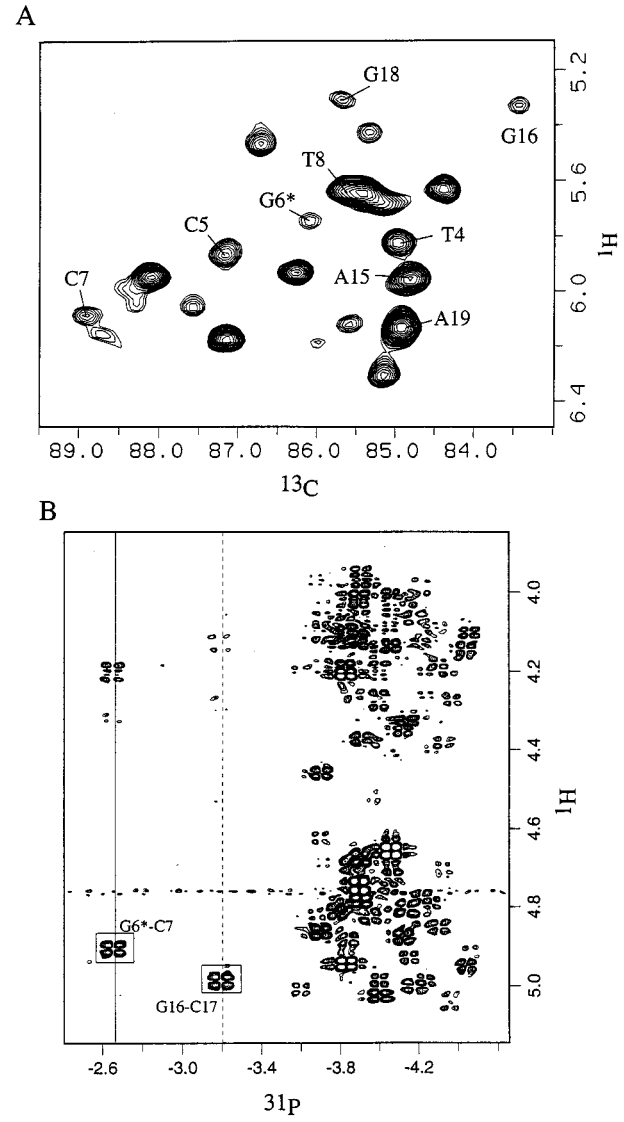

FIGURE 7: (A) An expanded contour-plot of natural abundance ^1H-^{13}C heteronuclear multiple-quantum coherence (HMQC) experiment on the [AF]dG·dC 11-mer duplex in D_2O buffer at 25 °C. The C1′ assignments are marked for residues in the d(T4-C5-[AF]G6-C7-T8)·d(A15-G16-C17-G18-A19) segment. (B) An expanded contour-plot of the proton-detected phosphorus-proton heteronuclear correlation experiment on the [AF]dG·dC 11-mer duplex in D_2O buffer at 25 °C. The phosphorus assignments are listed for the two downfield shifted resonances in the spectrum. The correlation cross-peaks between the phosphorus and its 5′-flanking sugar H3′ protons are boxed.

glycosidic torsion angle for the [AF]dG6 residue, which was not restricted to this value during the subsequent molecular mechanics computation. The AF-DNA orientation space was then searched with 16 energy minimization trials in which the linkage torsion angles α′ [[AF]dG6(N^9)-[AF]dG6(C^8)-[AF](N)-[AF](C^2)] and β′ [[AF]dG6(C^8)-[AF](N)-[AF](C^2)-[AF](C^1)] were each started at 0°, 90°, 180°, and 270° in all combinations. These 16 trials represent arbitrary unbiased high-energy starting orientations of the carcinogen that equally survey the potential energy surface of the adduct. Searching orientation space at 90° intervals of α′ and β′ is a robust procedure for locating all the important potential energy wells because our minimization protocol permits torsion angle variations of up to 100° in each minimization step (*22*). Consequently, energy minima in each quadrant

of α′ and β′ are accessible, and the reduced variable domain of torsion angle space greatly enhances the likelihood of finding the important structures.

Of the 16 structures computed, 11 structures exhibited good fit to the NMR data (eqs 1 and 2) and had the lower energies (Table S4). These 11 structures were identified as being in two different families in which the common features are that the aminofluorene ring of the [AF]dG adduct in a *syn* alignment intercalates between intact dC5·dG18 and dC7·dG16 base pairs, and the modified guanine and its partner dC17 are displaced into the major groove. However, the two families differ in the orientation of the modified guanine. Five structures have the modified guanine ring tilted toward the 5′-side of the modified strand, whereas it is tilted slightly toward the 3′-side of the modified strand in the other six structures. Although all 11 structures fit the NMR restraints, the structures which have the modified guanine ring tilted slightly toward the 3′ direction of the modified strand have lower energies (Table S4, Supporting Information). A view looking into the major groove and normal to the helical axis of the central trimer duplex segment showing the superposition within each of these two different families of structures is shown in Figure S1 (Supporting Information).

In addition, there are two rotameric orientations of the intercalated aminofluorene, namely with the C^9-containing edge of aminofluorene facing either the minor groove (six structures) or the major groove (five structures). Two structures, with low values for the goodness-of-fits functions and lower energies, from each class where the modified guanine ring is either tilted toward 5′-side (structures 3 and 5, Table S4) or toward 3′-side (structure 7 and 9, Table S4) of the modified strand) were embedded into an energy minimized B-form 11-mer duplex and reminimized with all restraints. Subsequently, the hydrogen-bond penalty function and the distance restraints were released with energy minimization in one step, yielding four final unrestrained minimum energy structures. Three of these unrestrained structures retained low goodness-of-fit indices.

A view looking into the major groove and normal to the helical axis of the central pentanucleotide duplex segment showing the superposition of these three structures is shown in Figure 8A, while a view looking down the helical axis of the central trimer segment showing the overlap geometry of the aminofluorene ring and flanking dC5·dG18 and dC7·dG16 pairs is shown in Figure 8B. Each of these three structures exhibits good agreement with the NMR data. In two of the three structures, the C^9-containing edge of the aminofluorene faces the minor groove, while in the third structure it faces the major groove. The pairwise root mean square deviation (rmsd) values of the d(T4-C5-[AF]G6-C7-T8)·d(A15-G16-C17-G18-A19) segment between the two structures with the same AF orientation is 0.49 Å, while the rmsd values between the two rotamers are 1.38 and 1.39 Å. One structure from each family is selected to represent the two rotamers and designated structure I (with the C^9-containing edge of the aminofluorene facing the minor groove) and structure II (with the C^9-containing edge of the aminofluorene facing the major groove).

The robustness of the above computational protocol could be checked by initiating the molecular mechanics calculations from a starting structure containing an *anti*-glycosidic torsion angle at the [AF]dG6 residue and monitoring whether the distance restrained DUPLEX computations facilitated an *anti* to *syn* transition at the modified guanine in the AF-intercalated conformer of the [AF]dG·dC 11-mer duplex. Such an experiment has been undertaken using the DUPLEX protocol discussed above with the results summarized in Table S5 (Supporting information). Significantly, nine of the 16 structures flipped from *anti* to *syn* alignment at [AF]-dG6 during the molecular mechanics computations, with lower F_N and F_{NN} goodness-of-fit indices, and lower energies observed for the alignments with a *syn* glycosidic torsion angle at the modified guanine in the AF-intercalated conformer (Table S5).

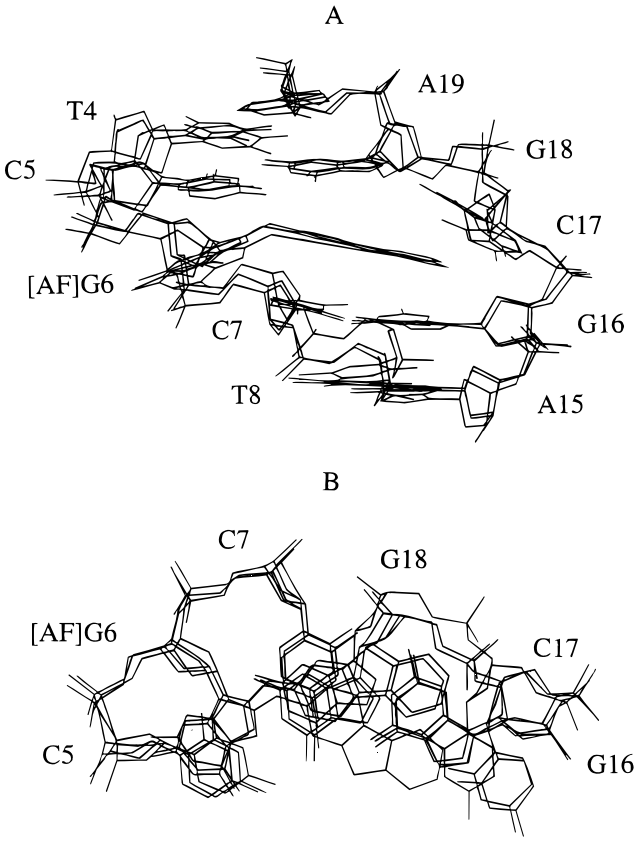

FIGURE 8: Superposition of the three d(T4-C5-[AF]G6-C7-T8)·d(A15-G16-C17-G18-A19) central five base pair segments that best fit the NMR data of the [AF]dG·dC 11-mer duplex obtained from the 16 trials to search conformational space using NMR restraints (Table 3) and the program DUPLEX. (A) View looking into the major groove and normal to the helix axis of the central 5-mer segments and (B) view looking down the helix axis of the central d(C5-[AF]G6-C7)·d(G16-C17-G18) segment.

Solution Structures. Views normal to the helix axis and looking into the major groove of the central d(T4-C5-[AF]-G6-C7-T8)·d(A15-G16-C17-G18-A19) segment of the NMR-molecular mechanics structures of the AF-intercalated conformer of the [AF]dG·dC 11-mer duplex are shown for structure I in Figure 9A and for structure II in Figure 10A. The corresponding structures for the entire duplexes are shown in Figures S2 and S3 (Supporting information), respectively. In both structures, the covalently linked aminofluorene ring intercalates between flanking Watson−Crick dC5·dG18 and dC7·dG16 base pairs by displacing the guanine ring of the *syn*-[AF]dG6 and its partner dC17 into the major groove (Figures 9A and 10A). The major groove face of the sugar ring of dC5 is positioned over the guanine

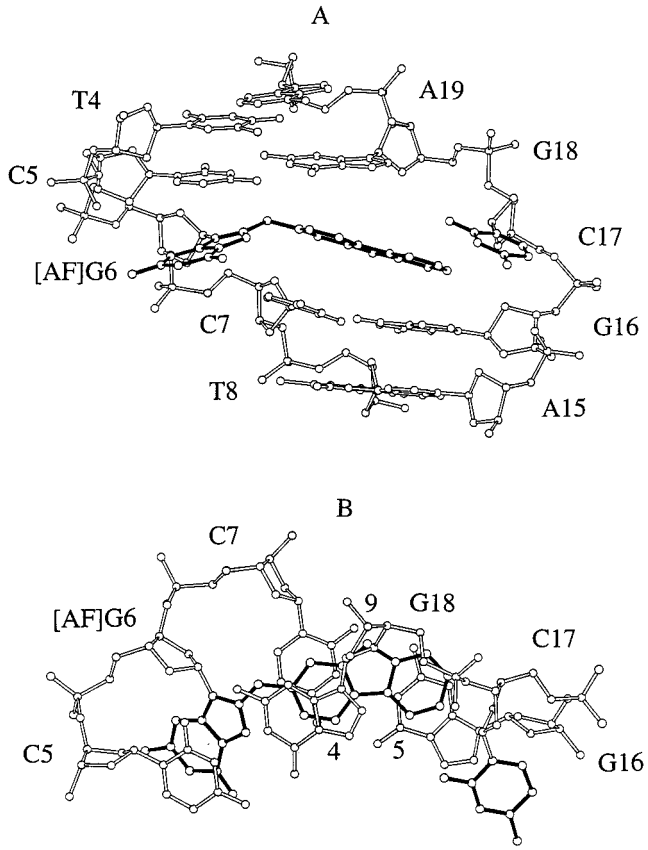

FIGURE 9: (A) View looking into the major groove and normal to the helix axis for the d(T4-C5-[AF]G6-C7-T8)·d(A15-G16-C17-G18-A19) segment of structure I of the [AF]dG·dC 11-mer duplex. The AF ring system is shown in darkened bonds and is intercalated between the dC5·dG18 and dC7·dG16 base pairs The modified dG6 and its partner dC17 bases are displaced into the major groove. (B) View looking down the helix axis for the d(C5-[AF]G6-C7)·d-(G16-C17-G18) segment of structure of the [AF]dG·dC 11-mer duplex. Note that the C^9 containing edge of AF is pointing toward the minor groove. Figures were prepared using Molscript V1.1 (*52*).

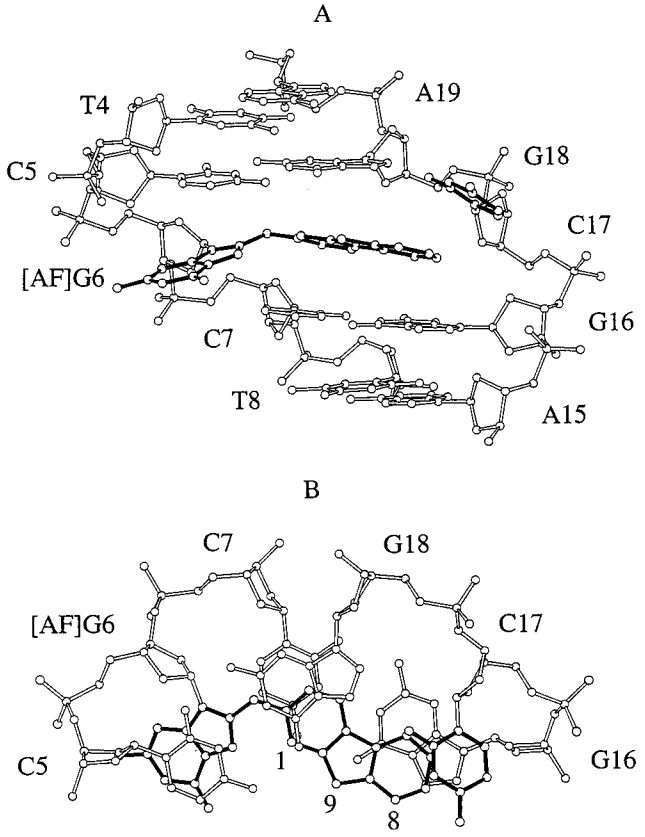

FIGURE 10: (A) View looking into the major groove and normal to the helix axis for the d(T4-C5-[AF]G6-C7-T8)·d(A15-G16-C17-G18-A19) segment of structure II of the [AF]dG·dC 11-mer duplex. The AF ring system is shown in darkened bonds and is intercalated between the dC5·dG18 and dC7·dG16 base pairs. The modified dG6 and its partner dC17 bases are displaced into the major groove. (B) View looking down the helix axis for the d(C5-[AF]G6-C7)·d-(G16-C17-G18) segment of structure II of the [AF]dG·dC 11-mer duplex. Note that the C^9 containing edge of AF is pointing toward the major groove. Figures were prepared using Molscript V1.1 (*52*).

base plane of the *syn*-[AF]dG6 which is tilted slightly toward the 3′-end of the modified strand for both structures (Figures 9A and 10A).

Views looking down the helix axis of the central d(C5-[AF]G6-C7)·d(G16-C17-G18) segment of the NMR-energy minimized structures of the [AF]dG·dC 11-mer duplex are shown for structure I in Figure 9B and for structure II in Figure 10B. These views emphasize the overlap geometry between the aminofluorene ring system and the flanking dC5·dG18 and dC7·dG16 base pairs. The long axis of the aminofluorene ring of AF is approximately parallel to the long axis of the dC5·dG18 and dC7·dG16 base pairs for both structures (Figures 9B and 10B). The carcinogen-base linkage site for the [AF]dG6 residue is defined by the torsion angles α' [[AF]dG6(N^9)-[AF]dG6(C^8)-[AF](N)-[AF](C^2)] and β' [[AF]dG6(C^8)-[AF](N)-[AF](C^2)-[AF] (C^1)]. These α', β' angles adopt values of 212° and 138° in structure I and of 197° and 323° in structure II. The $\beta' = 138°$ orientation directs the C^9-containing edge of aminofluorene toward the minor groove (Figure 9B), while the $\beta' = 323°$ value has this edge directed toward the major groove (Figure 10B) for the [AF]dG·dC 11-mer duplex. Thus, the pair of rotamers are related by an ~180° rotation about the AF long axis that is reflected in the β' values. The glycosidic torsion angles, sugar puckers, and backbone torsion angles for the d(T4-C5-[AF]G6-C7-T8)·d(A15-G16-C17-G18-A19) segment of the [AF]dG·dC 11-mer duplex are listed for structure I in Table S6 (Supporting Information) and for structure II in Table S7 (Supporting Information). The ψ(O4′-C1′-N9-C4) glycosidic torsion angle of the [AF]dG6 residue is *syn* in both rotamers, with values of $\chi = 65°$ in structure I and $\chi = 58°$ in structure II. Torsion angles and pseudorotation parameters for structure I and structure II are within or near ranges observed in B-DNA crystals (*36*) (Table S6 and S7).

DISCUSSION

Spectral Quality and Conformational Equilibrium. The line widths for both exchangeable (Figure 2A) and nonexchangeable (Figure 2B) proton resonances of the d(T4-C5-[AF]G6-dC7-T8)·d(A15-G16-C17-G18-A19) segment broaden (significant broadening observed for the dG16, dC17, and dG18 protons) on proceeding from the control 11-mer duplex to the [AF]dG·dC 11-mer duplex. The analysis of the NMR spectra is further complicated by the presence of exchange cross-peaks between major and minor conformers in slow exchange for the [AF]dG·dC 11-mer duplex (Figures 3 and 4). Despite difficulties associated with broadened and overlapped resonances, the analysis of the NOESY and TOCSY data sets have permitted the assignments of base and sugar protons in the AF-intercalated conformer, as well

as aminofluorene protons [with the exception of the AF-(NH) proton] of both conformers in the [AF]dG·dC 11-mer duplex.

The observation of exchange cross-peaks in the NOESY spectra of the [AF]dG·dC 11-mer duplex establish a slow equilibrium between the major conformer (~70%) in which the aminofluorene ring intercalates into the helix (which is the focus of this study), and a minor conformer (~30%) where the aminofluorene ring is external to the helix. The AF-external conformer could not be directly characterized in any detail, except for the assignment of the dG16 (12.78 ppm) and dG18 (12.45 ppm) imino protons and AF protons in this conformer. The aminofluorene protons for the minor AF-external conformer were collectively downfield shifted relative to those found in the AF-intercalated conformer (Figure 6) in which the aminofluorene ring experiences extensive stacking interactions with flanking dG·dC base pairs.

Conformational interconversion between equal populations of AF-external and AF-intercalated conformers was initially reported for the [AF]dG adduct in the d(A-[AF]G-G)·d(C-C-T) sequence context (*14*, *15*). Similar conformational heterogeneity has also been reported for the [AF]dG adduct in the d(T-[AF]G-A)·d(T-C-A) sequence context (*16*), where the predominant (~60%) conformer was of the AF-external type with the aminofluorene positioned in the major groove. It thus appears that the sequence context governs the distribution between AF-intercalated and AF-external conformers of the [AF]dG adduct positioned opposite dC at the duplex level.

Structural Features of the Major Conformer. The ~70% AF-intercalated conformer of the [AF]dG·dC 11-mer duplex has the AF moiety intercalated into the duplex, disrupting the potential pairing between [AF]dG6 and dC17 and displacing the modified *syn*-guanine and the complementary cytosine into the major groove (Figures 9 and 10). This is supported by the observation of several intermolecular NOEs between the imino protons of nonadjacent dG16 and dG18 residues and the protons located along different edges of the planar aminofluorene ring (Figures 3 and 4 and Table 3) in the adduct duplex. The NOEs between the superpositioned H6/H7 protons of AF and the base and sugar protons of dG16 and dC17 (Figure 4A and Table 3) are consistent with the orientation of the C^5-C^6-C^7-C^8 containing edge of aminofluorene toward the complementary strand in the NMR-molecular mechanics structures of the adduct duplex (Figures 9 and 10).

The observed proton chemical shift patterns for the AF-intercalated conformer (Table S3) can be explained by the overlap geometries between the aminofluorene ring and flanking dG·dC base pairs in the structure. The aminofluorene ring protons of the AF-intercalated conformer are sandwiched between flanking dG·dC base pairs (Figure 9 and 10) and should experience upfield ring current shifts (open circles, Figure 6) similar to those observed for the [AF]-dG·del 11-mer duplex (open squares, Figure 6) in which the AF moiety is also intercalated between the flanking base pairs (*12*). The plane of the intercalated aminofluorene ring is parallel to the planes of the flanking dG·dC base pairs and centered over the Watson−Crick hydrogen-bonding edges of the dC7·dG16 base pair in the AF-intercalated conformer of the [AF]dG·dC 11-mer duplex (Figures 9B and 10B). Consequently, the AF ring stacks better with the dC7·dG16 base pair than with the dC5·dG18 base pair in the AF-intercalated conformer of the [AF]dG·dC 11-mer duplex (Figures 9B and 10B). This is reflected in the observation of large upfield chemical shift changes for the imino and amino proton of the dC7·dG16 base pair and to a lesser extent for the dC5·dG18 base pair (Table S3).

Both the guanine ring of *syn*-[AF]dG6 and the cytosine ring of dC17 are displaced into the major groove, resulting in a loss of stacking interactions between these residues and the flanking dG·dC base pairs. This is consistent with the absence of NOE cross-peaks between the imino proton of [AF]dG6 and the imino protons of both its 3′-side dG16 and 5′-side dG18 neighbors for the AF-intercalated conformer (Figure 3B). In addition, the imino proton of [AF]dG6 should resonate at high field since it no longer participates in hydrogen-bonding interactions with its partner dC17, while the sugar and base protons of the looped out dC17 residue should experience large downfield shifts, relative to their corresponding values in the control duplex. We observe these expected chemical shift differences experimentally (Table S3), consistent with the structures of the AF-intercalated conformer of the [AF]dG·dC 11-mer duplex (Figures 9 and 10).

The dC17 residue is the least-defined segment in the NMR-molecular mechanics structure of the AF-intercalated conformer of the [AF]dG·dC 11-mer duplex. The broader line widths of the base and sugar resonances of dC17 suggests that this residue experiences a significant degree of conformational heterogeneity. In addition, this conformational heterogeneity appears to be monitored at its dG16 and dG18 neighboring residues, since the line widths of base and sugar resonances dG16 and dG18 in the AF-intercalated conformer are also broader than their counterparts in the control duplex.

Rotamer Interconversion of AF Ring. The NOE cross-peak patterns in our earlier study on the [AF]dG adduct opposite a −1 deletion site established the existence of two rotamers of the AF ring that rapidly interconvert on the NMR time scale between alignments where the C^9-containing edge is directed toward the major and minor grooves at the intercalation site (*12*). Such an NOE cross-peak pattern could not be monitored in the current study due to the broader line widths of AF(H1), AF(H3), and AF(H4) proton resonances and the overlapped AF(H6) and AF(H7) proton resonances in the [AF]dG·dC 11-mer duplex. An almost equal number of structures with comparable low values for the goodness-of-fit indices (Figure S1), obtained from the 16 trials to search conformational space using NMR restraints (Table 3), have the C^9-containing edge facing the minor and the major grooves. However, the limited number of intermolecular NOEs (Table 3) observed in this study on [AF]-dG opposite dC relative to that of [AF]dG opposite a −1 deletion (*12*) precludes unambiguous characterization of the interconversion between the two rotamers. At the present time, we can only conclude that both rotamers can satisfy the NMR based distance restraints for the [AF]dG·dC 11-mer duplex.

Conformation of the Modified Guanine and Comparison between Base-Displaced Intercalated-AF Conformers. The [AF]dG6 residue adopts a *syn* glycosidic alignment for interconverting AF-intercalated structures I (Figure 9) and

II (Figure 10) of the [AF]dG·dC 11-mer duplex. The [AF]-dG6 glycosidic torsion angle was set to either *syn* or *anti* at the start of the computations (but not restricted to this range during the computations). We observed a flip to the *syn* alignment during DUPLEX computations for nine of the 16 structures starting from an *anti* alignment at [AF]dG6, with the *syn*-containing structures exhibiting lower energies and goodness-of-fit indices (Table S4). By contrast, none of the structures starting from a *syn* alignment at [AF]dG6 flipped to the *anti* alignemnt during DUPLEX computations. Our marker for distingusihing *syn* from *anti* alignment at the [AF]-dG6 lesion site is primarily based on the unusually downfield chemical shift of the H2′ proton (3.71 ppm) of this modified guanine in the [AF]dG·dC 11-mer duplex (Figure 5). We attribute this downfield shift to the in-plane ring current contribution from the purine ring of the modified guanine in a *syn* alignment.

Recent NMR-based structural studies by Eckel and Krugh (*14*, *15*) identified an equilibrium between AF-external and AF-intercalated conformers in slow exchange for the case of [AF]dG positioned opposite dC in a duplex in the d(A-[AF]G-G)·d(C-C-T) sequence context. These authors concluded that intercalation of the AF residue resulted in base displacement of the modified guanine into the minor groove. They considered both *anti* and *syn* alignments for the [AF]-dG residue in the AF-intercalated conformer but eventually favored the *anti* alignment. The principle reason for this choice was their reasoning that the 10 ms interconversion time scale favored *anti* alignments for both the AF-intercalated and AF-external conformers (*14*, *15*). However, using relaxation measurements, chemical-shift considerations, and complete band shape calculations of the exchange process, Ippel and co-workers have revealed the existence of multiconformational states in the *anti*-*syn* equilibrium at a similar time scale in DNA hairpin loops (*37*). The conclusions of Eckel and Krugh (*14*, *15*) contrast with our demonstration of base displacement of the modified guanine in a *syn* alignment into the major groove for the AF-intercalated conformer for the case of [AF]dG positioned opposite a dC in the d(C-[AF]G-C)·d(G-C-G) sequence context (present study). It is our view that the barrier to interconversion between the [AF]dG6 (*syn*) alignment in the AF-intercalated conformer and [AF]dG6 (*anti*) alignment in the AF-external conformer (*18*) account for the slow exchange between the major and minor conformers of the [AF]dG·dC 11-mer duplex.

The AF modified guanine in the *syn* conformation, is displaced into the major groove for the AF-intercalated conformer in our study (Figures 9 and 10) in contrast with the minor groove displacement for the *anti* conformation of the adduct in the Eckel and Krugh (*14*, *15*) study. The upfield chemical shifts observed for the major groove facing H5 (−0.33) and H2′ (−0.33) proton resonances of dC5 as a result of stacking over the purine ring of the modified guanine positioned in the major groove offer additional support for the *syn* AF-intercalated conformer for [AF]dG positioned opposite dC at the duplex level.

Comparison of Aromatic Amine C^8-dG Adduct Structures Which Adopt Base-Displaced Intercalated Conformations. The NMR-molecular mechanics structure of the [AF]dG·-dC 11-mer duplex (present study) is very similar to the previously reported [AP]dG·dC 11-mer duplex structure (*28*) in the same sequence context in which the covalently attached aromatic ring intercalates between intact flanking dG·dC base pairs with concurrent displacement of the modified guanine and the complementary cytosine into the major groove. An important distinction concerns our observed formation of only the AP-intercalated conformer with no evidence for an AP-external conformer in equilibrium in the [AP]dG·dC 11-mer duplex (*28*). This difference between the [AP]dG adduct (100% AP-intercalated conformer) and the [AF]dG adduct (∼70% AF-intercalated conformer) may reflect the much greater stacking between the aromatic amine ring and flanking dG·dC base pairs for the larger pyrenyl ring compared to the smaller fluorenyl ring.

The aminofluorene ring also intercalates into the helix and displaces the modified guanine into the major groove for [AF]dG adducts positioned opposite −1 (*12*) and −2 (*13*) deletion sites in the d(C-[AF]G-C) sequence context. The key differences between the [AF]dG positioned opposite dC (present study) and deletion sites (*12*, *13*) are as follows: (1) the displaced modified guanine of *syn*-[AF]dG positioned opposite deletion sites is tilted toward the 5′-side of the modified strand while the displaced modified *syn*-guanine of [AF]dG positioned opposite dC is tilted, but to a lesser extent, toward the 3′-side of the modified strand (Figures 9 and 10); and (2) the dC7 from the modified strand and dG18 from the partner strand are positioned over each other in the [AF]dG·dC 11-mer adduct duplex (Figures 9 and 10) but not in the [AF]dG adduct opposite a −1 deletion site (*12*).

A base-displaced AAF-intercalated structure has also been reported for the [AAF]dG adduct positioned opposite dC in the d(C-[AAF]G-C)·d(G-C-G) sequence context which features a *syn* modified guanine displaced into the major groove with insertion of the fluorenyl moiety into the helix (*38*). It represents the major (∼70%) conformer in the equilibrium with the partner cytosine stacked into the helix rather than displaced into the major groove in this adduct structure. NMR studies (*39*) have also been undertaken on an [AAF]dG adduct in the context of a −2 deletion duplex at the *Nar*I mutational hotspot of *Escherichia coli* (*40*−*43*). There is considerable heterogeneity of conformers in the NMR spectra, but the overall features have been interpreted in terms of a major conformer (∼80%) containing a modified displaced guanine with the attached AAF intercalated into the helix (*39*). These [AAF]dG structures support the base displacement (*44*) or insertion-denaturation (*45*) models for AAF modified DNA.

Conformations of AF-Modified dG Adducts and Mutagenesis. There are now three groups of solution structures containing [AF]dG adducts that have been reported in the literature. In the context of a mismatch duplex, the modified guanine is in the *syn* orientation and stacks into the helix while the AF is sandwiched into the B-DNA minor groove and directed 3′ along the modified strand (*10*, *11*). These structures are relevant to the propensity of [AF]dG for inducing dG·dA and also dG·dG mismatches (*1*, *2*, *4*, *43*, *44*). In this context, it is interesting that the AF-intercalated *syn* base-displaced structure observed in the present study has also been observed for an AF-modified dG at a model template-primer junction at which there is no partner opposite the the [AF]dG adduct site (*48*). Moreover, we note the similarity in the $\alpha' = 197°$ and $\beta' = 323°$ torsion angles for the AF-intercalated *syn* base-displaced [AF]dG·dC 11-mer

structure II reported in the present study and the $\alpha' = 208°$ and $\beta' = 317°$ torsion angles for the *syn* [AF]dG opposite dA mismatched duplex reported previously (*10*). This suggests that an incoming dATP would be stabilized as it is in the mismatched duplex with very little rearrangement from the base-displaced AF-intercalated conformation observed in the present research and in the model template-primer junction (*48*).

In the context of −1 and −2 deletion duplexes, the [AF]-dG also adopts an alignment involving AF intercalation with base displacement of a *syn* modified guanine into the helical groove (*12*, *13*). In duplexes with the normal partner cytosine, one conformer contains normal *anti* modified dG, with the AF in the major groove with all base pairs intact and normal base stacking (*14*−*18*). Furthermore, in this type of context, a second conformer is observed with features of the major conformer in the present work, namely AF intercalation with base displacement of a *syn* modified guanine into the helical groove.

The feasibility of both *syn* and *anti* alignments for AF modified dG is in harmony with calculations reported previously (*25*, *49*, *50*). This contrasts with experimental observations (*38*) and calculations (*25*, *49*, *50*) for AAF modified dG, which indicate that the *syn* domain is markedly favored in this more hindered adduct. The remarkable heterogeneity of conformations manifested by the [AF]dG adduct, which is finely governed by the local base sequence context, is undoubtedly a key element governing its mutagenic properties. Moreover, structural relationships and distinctions between AF and AAF modified dG are likely to underlie the mutagenic differences between this pair of related adducts (*51*). The following paper in this issue (*18*) discusses these biological implications, especially in relation to mutagenesis by such adducts at the *Nar*I hotspot sequence of *E. coli*.

Coordinates. The coordinates of the *syn* AF-intercalated conformer of the [AF]dG·dC 11-mer are available on request from S.B., whose email address is broyde@nyu.edu.

ACKNOWLEDGMENT

We thank Marazban Dehnugara for his technical assistance and Zhengtian Gu for discussions on various aspects of this project.

SUPPORTING INFORMATION AVAILABLE

Seven tables listing the complete exchangeable and nonexchangeable proton chemical shifts for the [AF]dG·dC 11-mer duplex, chemical shift differences between the [AF]-dG·dC 11-mer duplex and control 11-mer duplex, energy and goodness-of-fit parameters of DUPLEX computed structures starting from *syn* and *anti* [AF]dG alignments and the backbone torsion angles for the central 5-mer segment, and three figures showing the superposition of 11 structures in two families derived following 16 energy minimization trials and the unrestrained structures of the entire adduct duplexes (14 pages). Ordering information is given on any current masthead page.

REFERENCES

1. Heflich, R. H., and Neft, R. E. (1994) *Mutat. Res.: Rev. Genet. Toxicol. 318*, 73−174.
2. Bichara, M., and Fuchs, R. P. P. (1985) *J. Mol. Biol. 183*, 341−351.
3. Gupta, P. K., Lee, M. S., and King, C. M. (1988) *Carcinogenesis 9*, 1337−1345.
4. Carothers, A. M., Urlaub, G., Mucha, J., Yuan, W., Chasin, L. A., and Grunberger, D. (1993) *Carcinogenesis 14*, 2181−2184 .
5. Melchoir, W. B. Jr., Marques, M. M., and Beland, F. A. (1994) *Carcinogenesis 15*, 889−899.
6. Tebbs, R. S., and Romano, L. J. (1994) *Biochemistry 33*, 8998−9006.
7. Ross, J., Doisy, R., and Tang, M. S. (1988) *Mutat. Res. 201*, 203−212.
8. Shibutani, S., and Grollman, A. P. (1993) *J. Biol. Chem. 268*, 11703−11710.
9. Hoffmann, G. R., and Fuchs, R. P. P. (1997) *Chem. Res. Toxicol. 10*, 347−359.
10. Norman, D., Abuaf, P., Hingerty, B. E., Live, D., Grunberger, D., Broyde, S., and Patel, D. J. (1989) *Biochemistry 28*, 7462−7476.
11. Abuaf, P., Hingerty, B. E., Broyde, S., and Grunberger, D. (1995) *Chem. Res. Toxicol. 8*, 369−378.
12. Mao, B., Cosman, M., Hingerty, B. E., Broyde, S., and Patel, D. J. (1995) *Biochemistry 34*, 6226−6238.
13. Mao, B., M., Hingerty, B. E., Broyde, S., and Patel, D. J. (1995) *Biochemistry 34*, 16641−16653.
14. Eckel, L. M., and Krugh, T. R. (1994) *Nat. Struct. Biol. 1*, 89−94.
15. Eckel, L. M., and Krugh, T. R. (1994) *Biochemistry 33*, 13611−13624.
16. Cho, B. P. Beland, F. A., and Marques, M. M. (1994) *Biochemistry 33*, 1373−1384.
17. Zhou, L., Rajabzadeh, M., Traficante, D. D., and Cho, B. P. (1997) *J. Am. Chem. Soc. 119*, 5384−5389.
18. Mao, B., M., Hingerty, B. E., Broyde, S., and Patel, D. J. (1998) *Biochemistry 37*, 95−106.
19. Marion, D., Ikura, M., Tschudin, R., and Bax, A. (1989) *J. Magn. Reson. 85*, 393−399.
20. Patel, D. J., Kozlowski, S. A., Nordheim, A., and Rich, A. (1982) *Proc. Natl. Acad. Sci. U.S.A. 79*, 1413−1417.
21. van der Ven, F. J., and Hilbers, C. W. (1988) *Eur. J. Biochem. 178*, 1−38.
22. Hingerty, B. E., Figueroa, S., Hayden, T., and Broyde, S. (1989) *Biopolymers 28*, 1195−1222.
23. Taylor, E. R., and Olson, W. K. (1983) *Biopolymers 22*, 2667−2702.
24. Hingerty, B. E., and Broyde, S. (1982) *Biochemistry 21*, 3243−3252.
25. Broyde, S., and Hingerty, B. E. (1983) *Biopolymers 22*, 2423−2441.
26. Schlick, T., Hingerty, B. E., Peskin, C. S., Overton, M. L., and Broyde, S. (1990) in *Theoretical Chemistry and Molecular Biophysics* (Beveridge, D., and Lavery, R., Eds.) pp 39−58, Academic Press, New York.
27. Cosman, M., de los Santos, C., Fiala, R., Hingerty, B. E., Ibanez, V., Luna, E., Harvey, R., Geacintov, N. E., Broyde, S., and Patel, D. J. (1993) *Biochemistry 32*, 4145−4155.
28. Mao, B., Vyas, R. R., Hingerty, B. E., Broyde, S., Basu, A. K., and Patel, D. J. (1996) *Biochemistry, 35*, 12659−12670.
29. Patel, D. J., Shapiro, L., and Hare, D. (1987) *Annu. Rev. Biophys. Chem. 16*, 423−454.
30. Cosman, M., Hingerty, B. E., Geacintov, N. E., Broyde, S., and Patel, D. J. (1995) *Biochemistry, 34*, 15334−15350.
31. Kettani, A., Kumar, R. A., and Patel, D. J. (1995) *J. Mol. Biol. 254*, 638−656.
32. Wang, Y., and Patel, D. J. (1995) *J. Mol. Biol. 251*,76−94.
33. Ghose, R., Marino, J. P., Wiberg, K. B., and Prestegard, J. H. (1994) *J. Am. Chem. Soc. 116*, 8827−8828.
34. Greene, K. L., Wang, Y., and Live, D. (1995) *J. Biomol. NMR 5*, 333−338.
35. Arnott, S., Bond, P. J., Selsing, E., and Smith, P. J. (1976) *Nucleic Acids Res. 2*, 2459−2470.

36. Berman, H. M., Olson, W. K., Beveridge, D. L., Westbrook, J., Gelbin, A., Demeny, T., Hsieh, S. H., Srinivasan, A. R., and Schneider, B. (1992) *Biophys. J. 63*, 751−759.
37. Ippel, J. H., Lanzotti, V., Galeone, A., Mayol, L., Van den Boogaart, J. E., Pikkemaat, J. A., and Altona, C. (1995) *Biopolymers 36*, 681−694.
38. O'Handley, F. F., Sanford, D. G., Xu, R., Lester, C. C., Hingerty, B. E., Broyde, S., and Krugh, T. R. (1993) *Biochemistry 32*, 2481−2497.
39. Milhé, C., Fuchs, R. P. P., and Lefevre, J.-F. (1996) *Eur. J. Biochem. 235*, 120−127.
40. Fuchs, R. P. P., Schwartz, N., and Daune, M. P. (1981) *Nature 294*, 657−659.
41. Fuchs, R. P. P. (1983) *J. Mol. Biol. 177*, 173−180.
42. Koffel-Schwartz, N., Verdier, J. M., Bichara, M., Freund, A. M., Daune, M. P., and Fuchs, R. P. P. (1984) *J. Mol. Biol. 177*, 33−51.
43. Burnouf, D., Koehl, P., and Fuchs, R. P. P. (1989) *Proc. Natl. Acad. Sci. U.S.A. 86*, 4147−4151.
44. Grunberger, D., Nelson, J. H., Cantor, C. R., and Weinstein, I. B. (1970) *Proc. Natl. Acad. Sci. U.S.A. 66*, 488−494.
45. Fuchs, R. P. P., and Daune, M. (1971) *FEBS Lett. 34*, 295−298.
46. Basu, A. K., and Essigmann, J. M. (1988) *Chem. Res. Toxicol. 1*, 1−18.
47. Gupta, P. K., Johnson, D. L., Reid, T. M., Lee, M.-S., Romano, L. J., and King, C. M. (1989) *J. Biol. Chem. 264*, 20120−20130.
48. Mao, B., Gu, Z., Gorin, A., Hingerty, B. E., Broyde, S., and Patel, D. J. (1998) *Biochemistry* (in press).
49. Lipkowitz, K. B., Chevalier, T., Widdifield, M., and Beland, F. A. (1982) *Chem.-Biol. Interact. 40*, 57−76.
50. Shapiro, R., Sidawi, D., Miao, Y. S., Hingerty, B. E., Schmidt, K. E., Moskowitz, J., and Broyde, S. (1994) *Chem. Res. Toxicol. 7*, 239−253.
51. Beland, F. A., and Kadlubar, F. F. (1990) in *Handbook of Experimental Pharmacology, Vol. 94/I: Chemical Carcinogenesis and Mutagenesis* (Cooper, C. S., and Grover, P. L., Eds.) pp 267−325, Springer-Verlag, Heidelberg.
52. Kraulis, P. J. (1991) *J. Appl. Crystallogr. 24*, 946−950.
53. Altona, C., and Sundaralingam, M. (1972) *J. Am. Chem. Soc. 94*, 8205−8212.

BI972257O